AGU PUBLICATIONS

Space Weather

RESEARCH ARTICLE
10.1002/2017SW001698

**Key Points:**
- An empirical, predictive model function is presented for electron fluxes for energies of 40, 75, and 150 keV at geostationary orbit
- Higher solar wind speed in general results in electron flux enhancements in energies 30–200 keV at geostationary orbit
- Negative IMF $B_Z$ at midnight to noon results in electron flux enhancements in energies 30–200 keV at geostationary orbit

**Correspondence to:**
I. Sillanpää,
ilkka.sillanpaa@fmi.fi

**Citation:**
Sillanpää, I., Ganushkina, N. Y., Dubyagin, S., & Rodriguez, J. V. (2017). Electron fluxes at geostationary orbit from GOES MAGED data. *Space Weather*, *15*, 1602–1614. https://doi.org/10.1002/2017SW001698

Received 26 JUL 2017
Accepted 9 NOV 2017
Accepted article online 14 NOV 2017
Published online 7 DEC 2017



# Electron Fluxes at Geostationary Orbit From GOES MAGED Data

**Ilkka Sillanpää[1], N. Yu. Ganushkina[1,2], S. Dubyagin[1], and J. V. Rodriguez[3]**

[1]Finnish Meteorological Institute, Helsinki, Finland, [2]University of Michigan, Climate and Space Sciences and Engineering, Ann Arbor, MI, USA, [3]Cooperative Institute for Research in Environmental Sciences, University of Colorado Boulder, Boulder, CO, USA

**Abstract** Electron behavior in energies below 200 keV at geostationary orbit has significance for satellite operations due to charging effects on spacecraft. Five years of keV energy electron measurements by the geostationary GOES-13 satellite's MAGnetospheric Electron Detector (MAGED) instrument has been analyzed. A method for determining flight direction integrated fluxes is presented. The electron fluxes at the geostationary orbit are shown to have significant dependence on solar wind speed and interplanetary magnetic field (IMF) $B_Z$: increased solar wind speed correlates with higher electron fluxes with all magnetic local times while negative IMF $B_Z$ increases electron fluxes in the 0 to 12 magnetic local time sector. A predictive empirical model for electron fluxes in the geostationary orbit for energies 40, 75, and 150 keV was constructed and is presented here. The empirical model is dependent on three parameters: magnetic local time, solar wind speed, and IMF $B_Z$.

**Plain Language Summary** Low-energy electrons in near-Earth space can be hazardous to satellites due to charging effects they may cause. Five years of low-energy electron data from the geostationary orbit of Earth by GOES-13 satellite was analyzed. The statistical analysis showed that low-energy electron fluxes were elevated by increased solar wind velocity for any position on the geostationary orbit. In addition, when the magnetic field carried by the solar wind was southward, the electron fluxes were elevated in about half the orbit, while on the other half the fluxes were not affected. A predictive model of low-energy electrons at geostationary orbit was built based on this data. A new empirical model was constructed to predict electron fluxes in energies between 30 and 200 keV at the different positions at the geostationary orbit. The model uses solar wind speed and magnetic field values to calculate the predicted electron fluxes.

## 1. Introduction

The populations of low-energy electrons (below 200–300 keV) and their variations in the Earth's inner magnetosphere are critically important for the magnetospheric dynamics. One of their obvious roles is being a seed population, further accelerated to MeV energies by various processes in the Earth's radiation belts (Boyd et al., 2016; Chen et al., 2007; Horne et al., 2005; Jaynes et al., 2015; Li et al., 2014; Turner & Li, 2008). Another important effect is that the low-energy electron flux is highly responsible for surface-charging effects on satellites (Davis et al., 2008; Garrett, 1981; Lanzerotti et al., 1998; Thomsen et al., 2013). Recently, Ma et al. (2016) showed with their simulation study that the scattering of low-energy electrons by chorus waves together with intense electric field spikes leads to higher fluxes in energies 10–100 keV in the outer radiation belt indicating an important source mechanism for keV electrons.

There have been some long time and even continuous measurements of low-energy electrons and ions by satellites in geosynchronous or geostationary orbits. Numerous studies have been published on the analysis and modeling based on these measurements as described below.

Early measurements made by geostationary satellites ATS-1 and 1976-059A (DPS F6) revealed general features through statistical studies (Baker et al., 1978; Lezniak & Winckler, 1970). In addition, the variations of electron anisotropies in keV energies were associated with geomagnetic activity and the flattening of the electron pitch angle distributions during substorm onsets in the night sector.

Korth et al. (1999) presented statistics for 1 year of proton and electron fluxes at geosynchronous orbit measured by three Los Alamos National Laboratory (LANL) satellites, using the data from the Magnetospheric

Plasma Analyzer (MPA) instrument, which covered the energy range from 1 eV/q to 40 keV/q (Bame et al., 1993; McComas et al., 1993). Organized as a function of the local time and the *Kp* index, the fluxes show distinct boundaries that were interpreted to be caused by global magnetospheric particle drifts in the presence of loss processes due to charge exchange of the ions and auroral precipitation of the electrons. The following study by Korth and Thomsen (2001) further confirmed that obtained statistical boundaries approximately match the Alfvén boundary crossings when calculated using simple representations of convective electric field (Stern, 1975; Volland, 1973) and dipole magnetic field.

Shi et al. (2009) statistically examined the geosynchronous energetic flux response as measured by LANL synchronous orbit particle analyzer, SOPA, to solar wind dynamic pressure enhancements. It was obtained that for low-energy electrons, the primary response to magnetospheric compression is an increase in flux at geosynchronous orbit. Li et al. (2005) found using daily solar wind and interplanetary magnetic field (IMF) data that solar wind speed enhancements result in higher electron fluxes at geosynchronous orbit; the optimal time delay was found to increase rapidly with energy from a couple of hours or less for 50–150 keV to 15–25 h for energies 250 keV and above.

Denton et al. (2005) and Thomsen et al. (2007) presented the LANL geosynchronous data set extended to more than a full solar cycle. Denton et al. (2005) identified dependencies in the average plasma properties at the geosynchronous orbit by studying MPA instrument data with respect to the *Dst* index, local time, storm phase, and solar cycle. For electrons their energy range was from 30 eV to about 45 keV. For low *Kp* indexes the electron density is typically highest in the midnight-dawn sector, while for $Kp > 7$ the electron density becomes high throughout the geosynchronous orbit. For electron temperatures, however, the largest average values are in the midnight-dawn sector and were not found to expand any further for higher *Kp* values beyond the extent found at $Kp = 4$. Thomsen et al. (2007) gave percentile values for particle fluxes in energies from 1 eV to 40 keV; particularly, the lowest measured energy electron and proton fluxes were even orders of magnitude larger than by the ATS-6 model used in satellite design.

Sicard-Piet et al. (2008) created a model for yearly electron fluxes between 1 keV and 5.2 MeV at the geostationary orbit by combining multiple satellite data sets; its usability is especially toward estimating charged particle doses for spacecraft and solar panel degradation. Another type of empirical model was created by Denton et al. (2015) from LANL geosynchronous satellite data using MPA instruments for energies from about 1 eV to 40 keV. The model provides flux probabilities as percentile values for given *Kp* index, magnetic local time (MLT), and solar activity index $F_{10.7}$ values. Kellerman and Shprits (2012) determined two-dimensional probability distributions functions dependent on solar wind speed and density using electron data from the LANL geosynchronous satellites in energies between 20 keV and 3.5 MeV. Their results showed that electron fluxes have a positive correlation with the solar wind speed, while middle- to high-energy fluxes show anticorrelation with the solar wind density.

Hartley et al. (2014) used MAGED 30–600 keV electron data of year 2011 from the GOES-13 geostationary satellite to determine the effect of solar wind speed and density on the electron density, temperature, and energy density at the geostationary orbit. They found that simultaneously elevated electron number density and temperature are usually preceded by fast solar wind speed about 24 h previous. They also presented predictive formulas for electron density, temperature, and energy density at geostationary orbit; especially, the electron density lower limit shows dependence on the solar wind speed from 12 to 48 h in advance.

There have been also studies focusing on the effects of high-speed solar wind events. In their study using over a hundred superposed high-speed stream epochs, Denton and Borovsky (2008) analyzed plasma behavior on the dayside geosynchronous orbit. It was found that magnetospheric convection is increased creating very dense plasma at geosynchronous orbit about 20 h after the convection onset. Turner et al. (2016) have used new observations of a substorm activity event by the Magnetospheric Multiscale mission, and they found that there was an upper energy cutoff for electron acceleration by betatron and Fermi mechanisms that increased from 130 to over 500 keV over five or more injections.

The studies cited above show the dynamic nature of the keV energy range electrons at geosynchronous orbit and how the understanding of their behavior and also dependence on various magnetospheric processes has increased over the past decade or so. While many studies have shown correlations between solar wind conditions and energetic plasma features within Earth's magnetosphere, it should be emphasized that it is through

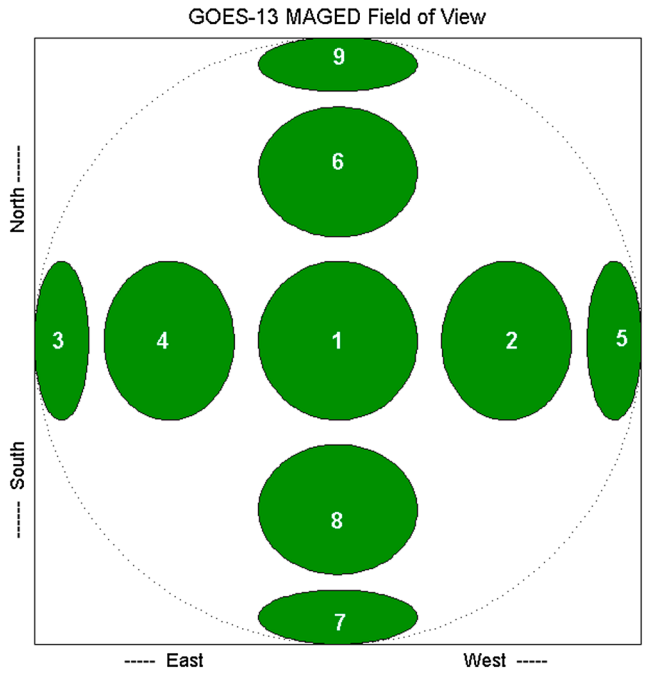


**Figure 1.** The fields of view of the MAGED telescopes (numbered green ellipses) as seen from the Earth and situated on a unit sphere projected onto a plane perpendicular to the earthward direction. Telescope 1 points in anti-Earth direction as seen from the Earth. Each telescope has a full detection cone angle of 30°.

a chain of processes that the solar wind affects, for example, electron flux enhancements at geosynchronous orbit. Namely, substorm injections and enhancements in magnetospheric convection and convection electric field are among the key mechanisms that directly affect energetic plasma in the inner magnetosphere and at geosynchronous orbit. It is in this context that our current study is taking a statistical look on the correlations between solar wind and interplanetary magnetic field and electrons at geosynchronous orbit in the tens to hundreds of keV energy range. Our purpose is to create a predictive empirical model for plasma conditions of low-energy electrons at geosynchronous orbit. We are building a model dependent only on parameters observed upstream of Earth. By using only solar wind and interplanetary magnetic field (IMF) parameters for the model and no geomagnetic or magnetospheric indices, we create a predictive model that can be run in real time.

The rest of the paper is organized as follows. In section 2 the GOES-13 MAGED instrument and data used in the study are described along with the method of determining flight direction integrated fluxes. Then the electron fluxes for a 5 year period are organized in section 3 by solar wind and IMF parameters and analysis results are described. In section 4 a new empirical model for electron fluxes in the geostationary orbit is presented for energies of 40, 75, and 150 keV along with the steps of its construction. Section 5 concludes the paper.

## 2. Flight Direction Integrated GOES MAGED Data

The MAGED (MAGnetospheric Electron Detector) instrument on board the GOES-13 satellite is a set of nine collimated solid state detectors (GOES N Series Data Book, 2010; Hanser, 2011; Rodriguez, 2014; Rowland & Weigel, 2012). The detectors operate in five energy channels of 30–50 keV, 50–100 keV, 100–200 keV, 200–350 keV, and 350–600 keV for electrons. The nine detectors, or telescopes, each with a full detection cone angle of 30°, form two crossing fans with the central telescope 1 pointing directly away from the Earth. Figure 1 shows their fields of view (numbered green ellipses) as seen from the Earth and situated on a unit sphere projected onto a plane perpendicular to the earthward direction. The orientation of the spacecraft is nominal in Figure 1.

The MAGED archival flux data are provided as differential electron fluxes determined for the midpoint of the five energy ranges (i.e., 40, 75, 150, 275, and 475 keV) and given separately for all nine telescopes. For the present study, we use the first three channels. The GOES-13 satellite is located on geostationary orbit at longitude of 75°W. GOES-13 has been kept in the nominal orientation since the start of its operation in May 2010.

In order to have one representative flux value for each energy instead of nine separate values from the nine telescopes, we determine flight direction integrated differential electron fluxes for each of the energies 40 keV, 75 keV, and 150 keV. The flight direction integrated flux is calculated in the case of the MAGED data similarly how the omnidirectional flux would be but it has an additional factor $\frac{1}{4\pi}$ and consequently also steradian (sr) in the units. For this, we use the directional differential fluxes of the nine telescopes and their pitch angles based on the magnetic field measurements by Magnetometer 1 on board GOES-13. The directional differential electron fluxes and pitch angles for each telescope are provided in the NOAA archival data (available at http://satdat.ngdc.noaa.gov/sem/goes/data/new_avg/).

The nine MAGED telescopes do not provide a full coverage of the full solid angle. Indeed, they provide a partial coverage on the hemisphere in the anti-Earthward direction. Furthermore, if the local magnetic field has a significant component along the Earth-satellite line, as when the near-field stretches prior to a particle injection, all the pitch angles from 0 to 180° cannot be covered by the telescopes. With this partial solid angle coverage, an integrated flux can still be obtained if we assume that the directional electron fluxes are (1) gyrotropic (i.e., fluxes are uniform in all directions with the same pitch angle) and (2) reflection symmetric with respect to the plane perpendicular to the magnetic field (i.e., fluxes for pitch angles $\alpha$ from 0 to $\pi/2$ are the same as from $\pi/2$ to $\pi$ or $J(\pi - \alpha) = J(\alpha)$). Therefore, in order to address the sparseness of samples in pitch

angle space, we replace those pitch angles $\alpha > \frac{\pi}{2}$ with $\pi - \alpha$, an operation we refer to as "folding," resulting in improved sampling between 0 and $\frac{\pi}{2}$. These assumptions represent an ideal case, which results from the Liouville's theorem when neither particle acceleration nor losses are considered. Åsnes et al. (2005) studied peaks in the electron pitch angle distributions at the geosynchronous orbit with LANL satellites in energies up to 47 keV and found the flux peaks consistently very symmetric. Thus, the assumptions seem to be justified for our purposes.

The nine MAGED telescopes actually provide a good pitch angle coverage of electron fluxes for any direction of the magnetic field when these two assumptions are accepted, and the calculation of flight direction integrated flux is simplified. It follows that a flight direction integrated differential flux $J$ for each energy channel can be determined by using the directional differential electron fluxes of individual telescopes to estimate the differential fluxes in all directions and then integrating these fluxes over the full solid angle of $4\pi$. The flight direction integrated flux in units of $1/(\mathrm{cm}^2\ \mathrm{s\ sr\ keV})$ is obtained using the following:

$$\begin{aligned} J &= \frac{1}{4\pi}\int_{4\pi} J(\Omega)\mathrm{d}\Omega \\ &= \frac{1}{4\pi}\cdot 2\pi \cdot 2\int_0^{\pi/2} J_{\mathrm{folded}}\,(\alpha)\sin(\alpha)\mathrm{d}\alpha \\ &= \sum_{i=1}^{n} J_i \int_{\alpha_{i0}}^{\alpha_{i1}} \sin(\alpha)\mathrm{d}\alpha \\ &= \sum_{i=1}^{n} J_i[-\cos(\alpha_{i0}) - (-\cos(\alpha_{i1}))] \end{aligned} \tag{1}$$

$$J_i = \frac{\sin(\alpha_{i0})\cdot J_{i0} + \sin(\alpha_{i1})\cdot J_{i1}}{\sin(\alpha_{i0}) + \sin(\alpha_{i1})}. \tag{2}$$

Here $J(\Omega)$ is the directional flux as function of the solid angle $\Omega$. $J_{i0}$ is the directional differential flux by a detector at the beginning of a folded pitch angle interval $i$, and $J_{i1}$ is the directional differential flux at the other end of the interval; the corresponding pitch angles are $\alpha_{i0}$ and $\alpha_{i1}$, respectively.

First, we move from integrating over solid angle $\Omega$ to integrating over folded pitch angles $\alpha$. Using assumption (A), we take the integrated flux over all directions with a given pitch angle $\alpha$ to be the product of the flux for that pitch angle and the circumference of the circle that pitch angle forms in directional space, namely, $2\pi \cdot \sin(\alpha)$. Furthermore, assumption (B) gives that the integration over pitch angles from 0 to $\pi$ is twice the integration over folded pitch angles from 0 to $\pi/2$, and hence, we have a factor $4\pi$. Then to discretize the integration over fluxes of the folded pitch angles $J_\alpha$ to the actual pitch angles of the telescopes, we use fluxes $J_i$ for each pitch angle interval $i$. These interval fluxes $J_i$ are given in equation (2) as weighted telescope fluxes with the circumferences (i.e., $2\pi \cdot \sin(\alpha)$; the $2\pi$ terms cancel in the ratio) at the end points of the interval $i$. These circumferences are directly proportional to the solid angle contributions of the telescope fluxes at the end points.

If there are any pairs of telescopes that have their folded pitch angles closer than 5° from each other, we replace the fluxes of these two telescopes with the mean flux of the two. This allows the integration over longer intervals to be weighted by the fluxes measured by several telescopes. The differential fluxes for the end points of 0 and $\pi/2$ are set to be the same as differential fluxes of the telescopes with lowest and highest folded pitch angles, respectively.

## 3. Electron Fluxes at Geostationary Orbit in 30–200 keV Energy Range

The GOES-13 MAGED data for a 5 year period between 1 January 2011 and 31 December 2015 were analyzed in three lower energy channels using 5 min averages of electron flight direction integrated fluxes determined with the method described in the previous section. The three lower energy channels centered on 40, 75, and 150 keV provided continuous coverage in the energy range from 30 to 200 keV. The MAGED data as 5 min average fluxes are at least 2 orders of magnitude above the single count flux levels throughout the 5 year period. In the following we describe our main results with this 5 year data set.

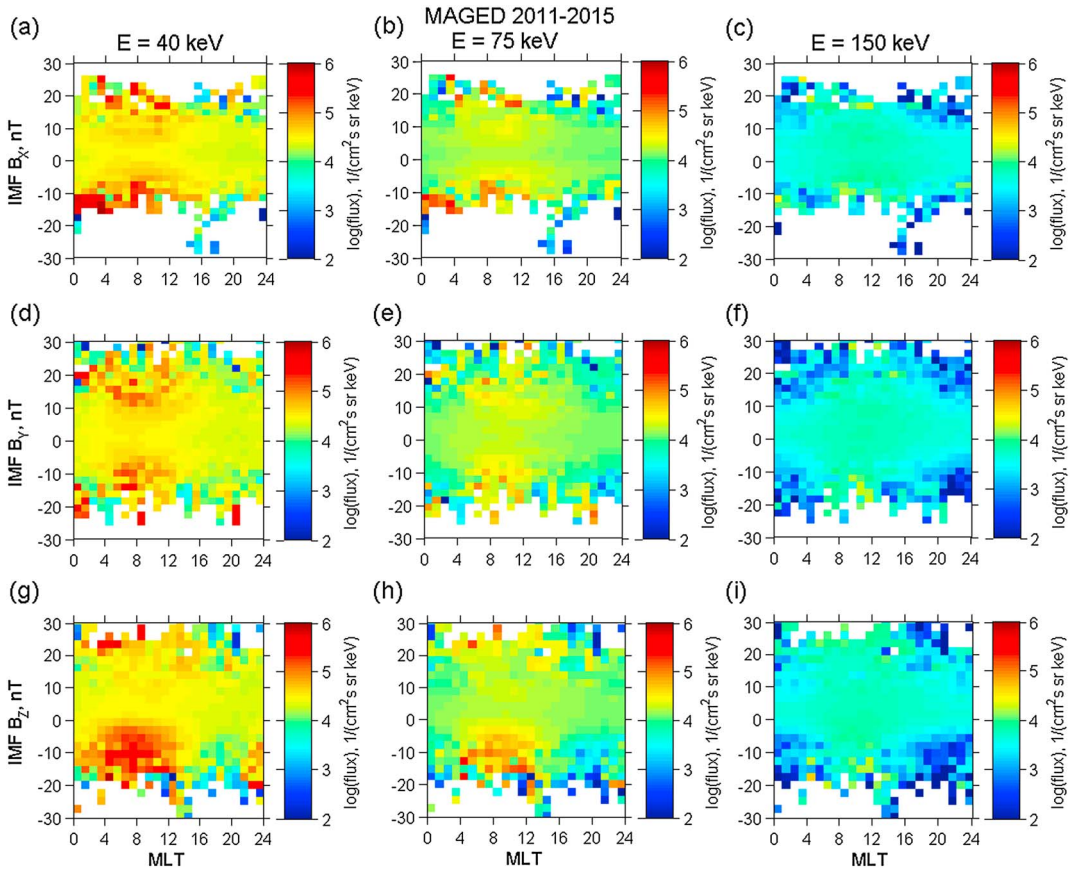


**Figure 2.** MAGED fluxes of energies 40, 75, and 150 keV organized with IMF components (a–c) $B_X$, (d–f) $B_Y$, and (g–i) $B_Z$. Bin values are medians of the data points.

We have organized the MAGED fluxes by the coincident solar wind and interplanetary magnetic field (IMF) parameters, including solar wind pressure, density, speed, and temperature and IMF components as provided by the OMNIWeb service of the Space Physics Data Facility at the Goddard Space Flight Center (http://omniweb.gsfc.nasa.gov/, provided as propagated values at the nose of the magnetopause).

Figure 2 shows median electron fluxes as functions of MLT and the IMF components $B_X$ (a–c), $B_Y$ (d–f), and $B_Z$ (g–i). The differential electron fluxes for energy 40 keV are about an order of magnitude higher than those of energy 150 keV with fluxes of energy 75 keV in between. Overall, the data show quite similar features for all three energies while the average flux levels are different. The $B_X$ values are mostly between −20 and 22 nT, whereas $B_Y$ and $B_Z$ reach absolute values up to 35 nT (however, the plots are limited to a range between −30 and 30 nT to show the main features). The fluxes in each bin show no sharp changes near the 0 nT lines in all the panels where the number of data points per bin is the highest. The variability of the median bin values clearly increases with the distance from the 0 nT lines as the number of data points per bin decreases.

In all the panels the average fluxes are higher in the postmidnight and dawn MLT sectors. The highest flux values are nearly symmetrical with respect to the $B_X = 0$ and $B_Y = 0$ lines above 5 nT and below −5 nT in these sectors. With $B_Z$ the high fluxes are especially concentrated in a large area in the night-dawn sector with $B_Z$ values less than −5 nT. In $B_X$ panels for energies 40 and 75 keV (Figures 2a and 2b) an asymmetric flux intensification is seen at the 0 to 4 MLT sector and $B_X < -10$ nT, though the feature may not be statistically significant. In the afternoon and dusk MLT sectors there are no significant changes in the average fluxes as functions of IMF component values.

The solar wind parameters speed $V_{SW}$, density $n_{SW}$, pressure $p_{SW}$, and temperature $T_{SW}$ are used to organize the MAGED fluxes in Figure 3. The organization of MAGED fluxes by the solar wind speed (Figures 3a–3c) shows nearly monotonic increases in the electron fluxes with increasing speed from about 250 to 800 km/s for each

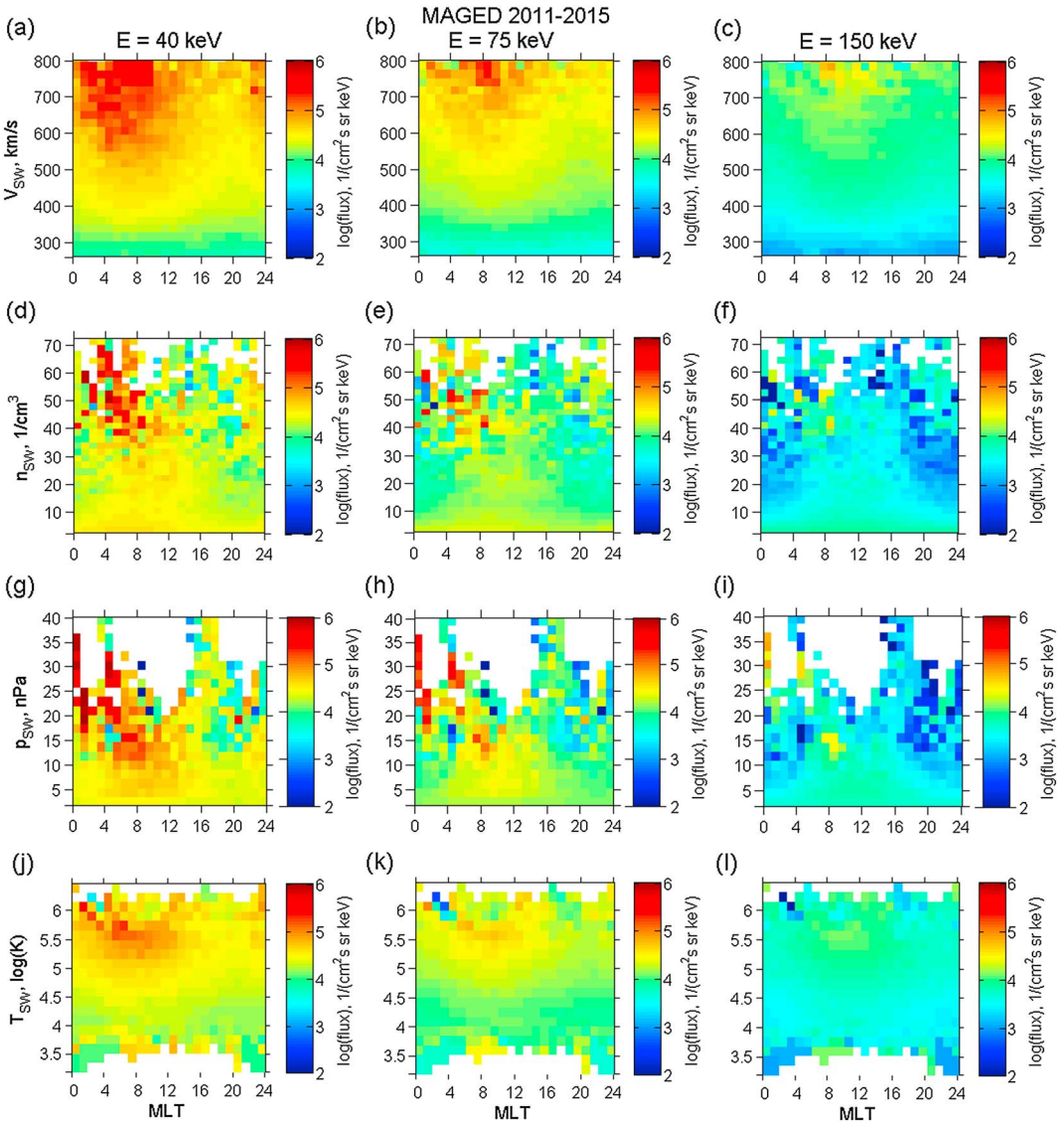


**Figure 3.** MAGED fluxes of energies 40, 75, and 150 keV organized with solar wind parameters (a–c) speed $V_{SW}$, (d–f) density $n_{SW}$, and (g–i) pressure $p_{SW}$. Bin values are medians of the data points.

of the three energies and each MLT hour; the highest median fluxes are found in the range of 2 to 10 MLT with solar wind speed above 700 km/s. Additionally, a sinusoidal shape in the logarithmic fluxes can be seen with 24 MLT hours corresponding to $2\pi$ of a full sine period. There is a notable shift in the phase of the sinusoidal behavior with the electron energy, with the flux maximum of $V_{SW} = 400$ km/s at around 5, 7, and 9 MLT for energies 40, 75, and 150 keV, respectively.

There is considerable similarity between solar wind speed (Figures 3a–3c) and the solar wind temperature (Figures 3j–3l): both have clear trends toward higher fluxes with higher parameter values nearly in all MLTs. Solar wind density (Figures 3d–3f) and pressure (Figures 3g–3i) show that higher density or pressure have a slight tendency to correspond to higher median fluxes in the dawn sector. However, this is not the case in other MLT sectors. For example, the 12 to 17 MLT sector shows almost no discernible features in the electron fluxes as organized with the solar wind density or pressure in all three energies (except at the highest density or pressure values where the number of data points per bin is very low). While there are distinct low flux features around density of 30 cm$^{-3}$ and in pressure 10–20 nPa in the premidnight sector, they are not statistically very significant due to the relatively low number of data points per bin at those parameter values.

## 4. Empirical Model for Electron Fluxes at Geostationary Orbit for Energies 40, 75, and 150 keV

Based on 5 years (2011–2015) of GOES-13 MAGED data, we have developed an empirical model for electron fluxes at the geostationary orbit for energies 40 keV, 75 keV, and 150 keV. The main aspects of the construction of the model are explained in the following.

The electron fluxes used were 5 min averaged flight direction integrated MAGED data from the GOES-13 satellite. The coincident solar wind and IMF parameters (provided by the OMNIWeb service of the Space Physics Data Facility) were studied to determine their correlation with the electron fluxes measured by GOES-13. The requirement of coincident solar wind and IMF data reduced the number of MAGED 5 min data points that could be used in years 2011–2015 from 520,000 to 464,000. This was due to missing ACE solar wind and/or IMF data. There was a small, statistically insignificant number of data points (123) with $V_{SW}$ higher than 800 km/s mostly in the dawn sector that were excluded from the data set. A continuous solar wind speed coverage in MLT hours was found to extend from the lowest data set values of about 250 to about 800 km/s with $V_{SW}$ bin width of about 30 km/s. (See Figures 3a–3c.)

Plots with the MAGED electron fluxes organized with solar wind and IMF parameters and MLT (e.g., Figures 2 and 3) were used to visually examine potential ways to construct the model function (i.e., looking for features in the plots that could be modeled with simple functional forms). In addition, linear correlation coefficients (CC) were calculated between solar wind speed, pressure, density, and temperature as well as with IMF components for the MAGED fluxes for energies 40, 75, and 150 keV. The highest correlation coefficients by far are with the solar wind speed: 0.3059, 0.3492, and 0.4191 for energies 40, 75, and 150 keV, respectively. The MAGED fluxes showed sinusoidal-like behavior with MLT when organized by $V_{SW}$ as described in the previous section. Other parameters show significantly lower correlations with MAGED data. The parameters that have absolute CC larger than 0.1 with the MAGED data are IMF $|B|$ in energies 40 and 75 keV (0.136 and 0.11, respectively), IMF $B_Z$ in energies 40 and 75 keV (−0.158 and −0.115), $n_{SW}$ in energy 150 keV (−0.163), $p_{SW}$ in energies 40 and 75 keV (0.118 and 0.104), and $T_{SW}$ in all energies (0.188, 0.203, and 0.197).

While solar wind speed seemed a promising base for the empirical model, more parameters were needed to create a viable model. The solar wind temperature has the second highest absolute CC with MAGED data; however, it has a strong correlation with the solar wind speed (CC = 0.628) and that meant that it was not likely to be a suitable parameter to use in addition to the solar wind speed. Three test functions were created of the form $a \cdot 10^{b \cdot V_{SW} \cdot \sin(\frac{\pi}{12} \cdot \mathrm{MLT} + c) + d}$ for three lower MAGED energies. The test function residuals of the MAGED data were used to search for additional model parameters. Other solar wind and IMF parameters were studied for viability by calculating their CC and plotting the MAGED data or the test function residuals organized by that parameter. Negative IMF $B_Z$ component values in the postmidnight and dawn sectors correlated with increased electron fluxes. This is seen as a wide peak centered around −10 nT in Figure 2. Both solar wind density and pressure plots showed some enhancements of electron fluxes (see Figure 3), but the residuals from the $V_{SW}$ test functions showed only weak enhancements, if any, as the density and pressure did not provide meaningful additions to the flux patterns in the test functions based on organization by the solar wind speed. Tests conducted by building model functions based on solar wind density or pressure combined with IMF $B_Z$ component peak failed as the resulting CC between MAGED data and the values from such test functions were significantly lower than with the solar wind speed test functions.

The best combination for model functions as per CC was found by combining solar wind speed and IMF $B_Z$ features. The empirical model functions were built based on the sinusoidal shape in the electron flux responses to the solar wind speed and added with a flux peak near dawn sector MLT for negative $B_Z$. The fitting routines used were iterative least squares algorithms.

The final functional form for the empirical model was found as presented below. The empirical model function provides flight direction integrated differential electron fluxes $f_{EMP}$ (in units of 1/(cm$^2$ s sr keV)) at geostationary orbit as

$$f_{EMP} = a1 \cdot 10^{V_{SW} \cdot (a2 \cdot \mathrm{sMLT} + a3 \cdot \mathrm{cMLT} + a4)} + b1 \cdot \exp\left[ -\frac{12 - |\,|\mathrm{MLT} - b2| - 12|}{b3} - \left( \frac{B_Z + 11}{8} \right)^3 \right] + c1, \quad (3)$$

**Table 1**
*Coefficients of the Empirical Model for Electron Fluxes at the Geostationary Orbit*

| Parameter | 40 keV | 75 keV | 150 keV |
|---|---|---|---|
| a1 | 8 500 | 76 000 | 15 000 |
| a2 | $3.3 \times 10^{-4}$ | $4.5 \times 10^{-5}$ | $2.6 \times 10^{-5}$ |
| a3 | $1.7 \times 10^{-4}$ | 0 | $-5 \times 10^{-5}$ |
| a4 | $1.8 \times 10^{-3}$ | $5 \times 10^{-4}$ | $5 \times 10^{-4}$ |
| b1 | 299, 000 | 97, 700 | 11, 100 |
| b2 | 6.4 | 7.8 | 8.4 |
| b3 | 4.9 | 4.6 | 2.9 |
| c1 | −19, 300 | −98, 600 | −19, 000 |

where

$$\mathrm{sMLT} = \sin\left(\frac{\pi}{12} \cdot \mathrm{MLT}\right), \tag{4}$$

$$\mathrm{cMLT} = \cos\left(\frac{\pi}{12} \cdot \mathrm{MLT}\right). \tag{5}$$

The model inputs are the MLT (corresponds to a set time and location on a geostationary orbit), the IMF $B_Z$ and the solar wind speed $V_{SW}$. MLT is given in hours, $B_Z$ is in units of nT, and $V_{SW}$ in km/s. Term $12-||\mathrm{MLT}-b2|-12|$ is the shortest time difference between MLT and parameter b2 (0 and 24 h in MLT are the same).

A further inspection revealed that a time delay of 1.5 h for the solar wind speed and $B_Z$ significantly improved the empirical model. Time delays between 0 and 3 h were fitted and tested separately for input parameters $B_Z$ and $V_{SW}$; the highest CC with MAGED data were clearly with a time delay of 1.5 h for $B_Z$. The time delays for $V_{SW}$ with the highest correlations were found between 1 and 2 h, each energy having different trend as a function of time delay. With the 1.5 h delay for both of these parameters, CC between the electron fluxes of the empirical model and MAGED data are 0.567, 0.504, and 0.486 for the MAGED energies of 40, 75, and 150 keV, respectively, for the time period 2011–2015. The prediction efficiencies are 0.321, 0.206, and 0.229 for the energies 40, 75, and 150 keV, respectively, showing that the model's performance is superior to averages of the MAGED data. Without any time delay for the solar wind speed and IMF the CC would be lower by 0.076 for the 40 keV energy, by 0.056 for 75 keV, and by 0.018 for 150 keV. Therefore, the IMF and solar wind speed values used are delayed by 1.5 h in the final model; that is, $V_{SW} = V_{SW}(t + 1.5\ \mathrm{h})$, $B_Z = B_Z(t + 1.5\ \mathrm{h})$, $\mathrm{MLT} = \mathrm{MLT}(t)$, and $f_{EMP} = f_{EMP}(t)$, where $t$ is time.

A realization that helped in reducing the number of energy-dependent parameters to eight in the model (see Table 1) was that three originally energy channel-dependent parameters could be replaced with constants in the exponent function of the $B_Z$ term resulting in term $\left((B_Z + 11)/8\right)^3$; these values (11, 8, and 3) determine the location (as in −11 nT), width scale (8 nT), and shape (with the exponent of 3) of the flux peak for negative $B_Z$ values. The final model coefficients for three energies are provided in Table 1.

Table 2 presents CC for each 6 h MLT sector in comparison to the overall CC. For the 0 to 6 MLT sector, CC between MAGED electron fluxes and the model results are significantly higher than the overall values. The evening to midnight sector (18–24) also has somewhat higher CC, while the lowest CC are in the prenoon sector 6–12. That the nightside MLT sectors and especially the postmidnight sector have higher CC is explainable with the low-energy electron source from the magnetospheric tail driven by solar wind affecting these sectors most directly via enhanced convection and substorm injections (e.g., Birn et al., 1998; Ganushkina et al., 2013).

The empirical model was tested with the GOES-13 MAGED data of the first 4 months of year 2016, which was not included in model development. The test period had 34,542 MAGED data points as 5 min averages and 30,942 data points that coincided with available solar wind and IMF measurements. For this period, the correlation coefficients between empirical model results and the MAGED electron fluxes are 0.548, 0.489, and 0.499 and prediction efficiencies (PE) 0.294, 0.219, and 0.2027 for energies 40, 75, and 150 keV, respectively. These CC and PE values vary a little from those obtained for the 5 year period that the model construction was based on; the differences in CC are only 0.02 or less.

**Table 2**
*Linear Correlation Coefficients Between the Empirical Model and MLT Quadrants and All Data for Energies 40, 75, and 150 keV*

| MLT sector | 40 keV | 75 keV | 150 keV |
|---|---|---|---|
| 0–6 | 0.603 | 0.556 | 0.527 |
| 6–12 | 0.520 | 0.430 | 0.444 |
| 12–18 | 0.561 | 0.504 | 0.475 |
| 18–24 | 0.583 | 0.516 | 0.489 |
| all | 0.567 | 0.504 | 0.486 |

Figure 4 shows the MAGED electron flux values against the electron fluxes given by the empirical model for 40 (a), 75 (b), and 150 keV (c) for the 5 year period of data used in the model construction and similar plots for the 4 months of the test period (d–f). There is a noticeable feature, especially in the plots of energies 75 and 150 keV, of an overestimation of low MAGED flux values by the model. The modeled fluxes are $10^4$–$10^6$ 1/(cm$^2$ s sr keV) for 75 keV and between $10^3$ and $10^4$ 1/(cm$^2$ s sr keV) for 150 keV when the corresponding observed fluxes were less than $10^3$ and $5 \cdot 10^2$ 1/(cm$^2$ s sr keV), respectively. For the highest values of the observed fluxes the model underestimates the measured electron fluxes: this is most pronounced for 75 keV energy around $5 \cdot 10^5$ 1/(cm$^2$ s keV) and for 150 keV energy above $5 \cdot 10^4$ 1/(cm$^2$ s keV) in MAGED flux values. The test period results from early 2016 (Figures 4d–4f) exhibit very similar features.

The empirical model mostly failed to capture the low flux tails of MAGED data as seen in Figure 4. To better understand possible underlying reasons for the low flux tails, we present Figure 5 that organizes the low fluxes with MLT and the declination of Sun. The declination of the Sun (or subsolar latitude) parametrizes Earth's seasonally varying tilt with respect to the Sun. Together with MLT, the declination of the Sun organized well the low flux data. The upper cutoff limits of the fluxes shown ($2 \cdot 10^3$, $5 \cdot 10^2$, and 50 1/(cm$^2$ s sr keV) for 40, 75, and 150 keV, respectively) were set so that the number of data points below the limit was close to each other for each of the three energies (between 3,229 and 3,353 data points).

Figure 5 shows that the lowest fluxes are concentrated to the nightside between 18 and 4 MLT. The frequency of low fluxes peaks sharply at the highest declination values (> 21°, that is, June and most of July), with highest numbers of data points right before midnight (maximum number of data points per bin were between 155 and 180 for the three energies). There seems to be a trend for these low fluxes to occur more frequently with positive declination than with negative.

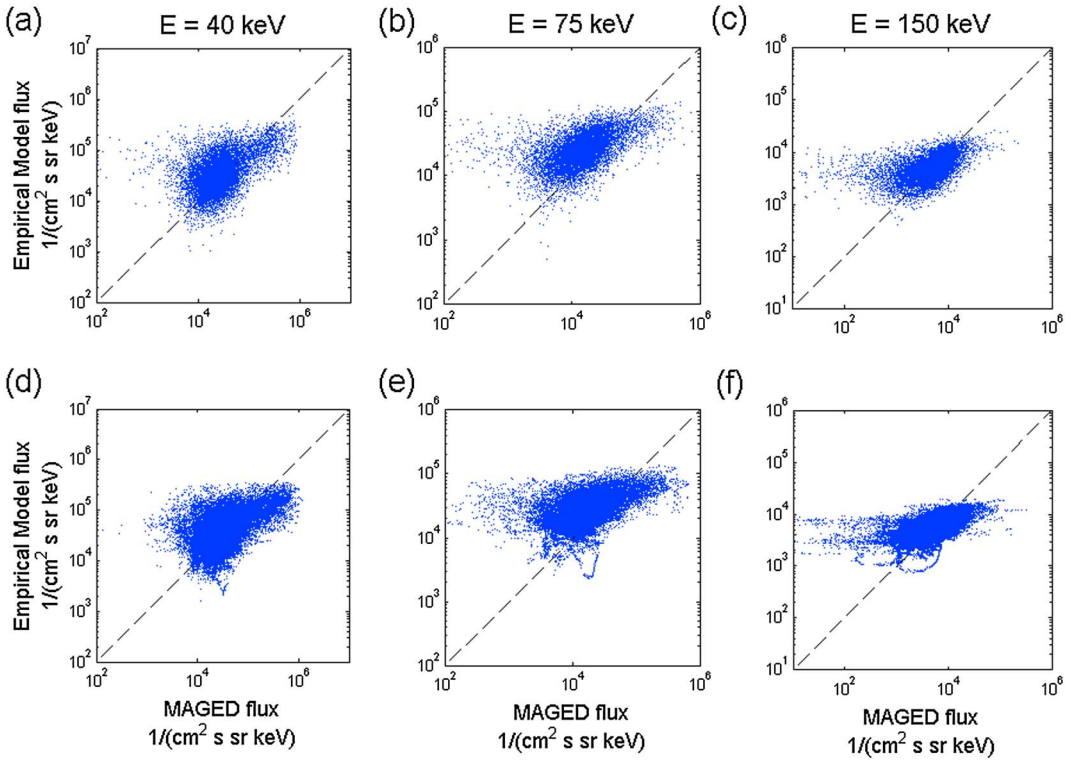


**Figure 4.** MAGED electron flux versus the electron fluxes given by the empirical model for (a) 40, (b) 75, and (c) 150 keV for period 2011–2015 with every fiftieth data point shown. (d–f) The MAGED electron flux versus the empirical model results for a 4 month test period January–April 2016 with all data points shown.

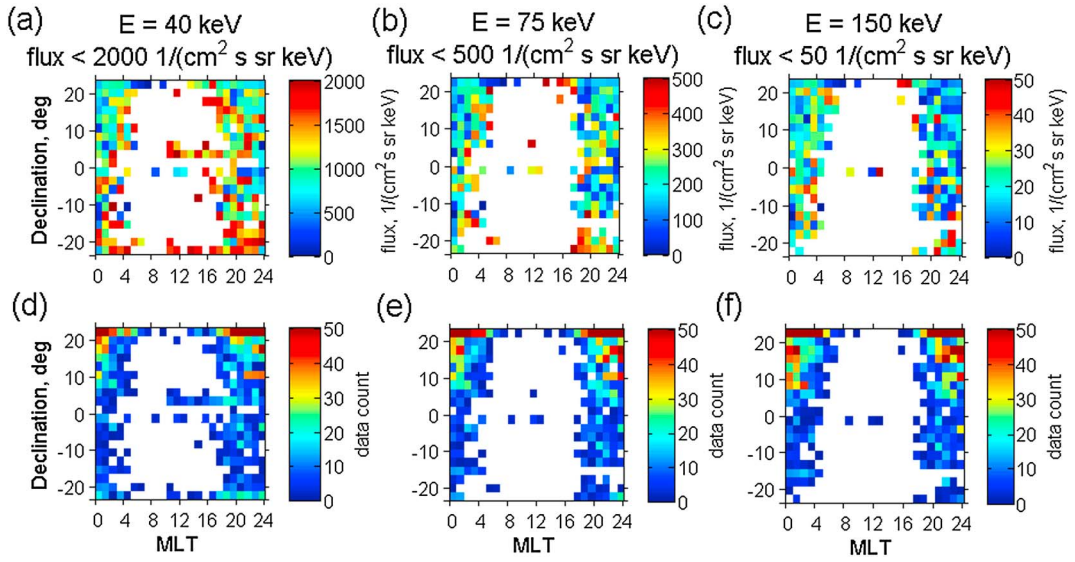


**Figure 5.** Low values of MAGED electron fluxes are shown against MLT and the declination of the Sun as (a–c) medians and as (d–f) the number of data points per bin for the 2011–2015 period. The upper limits of the flux values for the accepted data points were $2 \cdot 10^3$, $5 \cdot 10^2$, and 50 1/(cm$^2$ s sr keV) for 40, 75, and 150 keV, respectively. White areas are bins without any assigned data points.

Additional tests showed some improvement in CC between the MAGED data and the empirical model when criteria for omission of high-declination data points in the night sector were used in order to reduce the influence of the low flux tails. However, any tried criteria, that excluded most of the low flux data points defined by the low flux limits given above, removed also more than $6 \cdot 10^4$ other data points (about 14% of all data).

Figures 6a–6c show the MAGED data organized by IMF $B_Z$ and MLT and compared with the empirical model results (Figures 6d–6f) for the same time period from January 2011 to December 2015. Figure 7 presents similar comparison but with the electron fluxes organized solar wind speed $V_{SW}$ and MLT. These parameters, IMF $B_Z$, $V_{SW}$, and MLT, are all the input parameters used in the developed empirical model. The bin size used in the panels for modeled fluxes is smaller to demonstrate the patterns even with small number of data points. The modeled fluxes successfully replicate the main patterns of the electron flux data. The bin values are averages of the fluxes as that correspond well with the root-mean-square fitting done for the model.

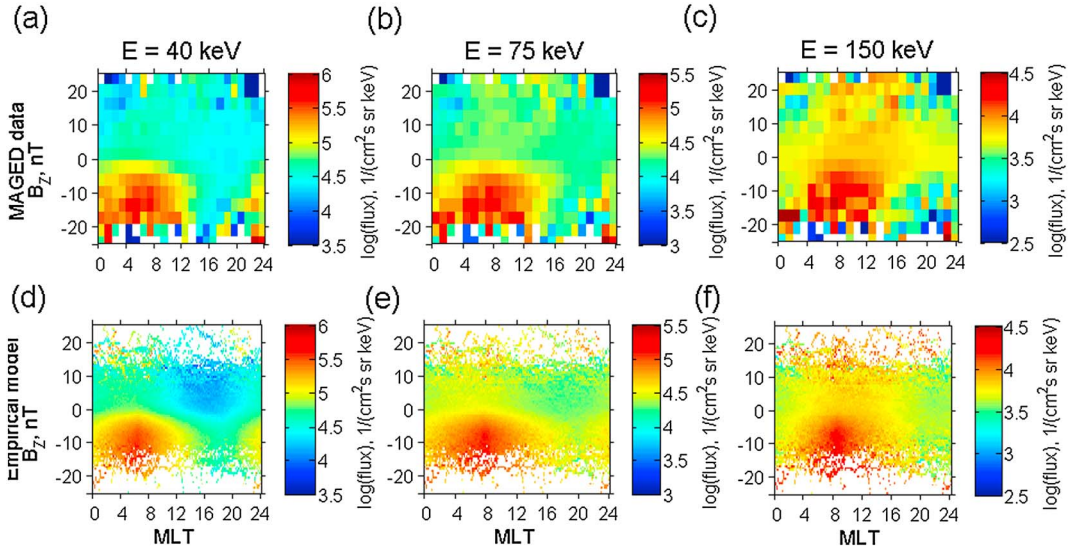


**Figure 6.** (a–c) MAGED data as dependent on IMF $B_Z$ and MLT compared with (d–f) the empirical model results for the same time period from January 2011 to March 2015. Bin values are averages.

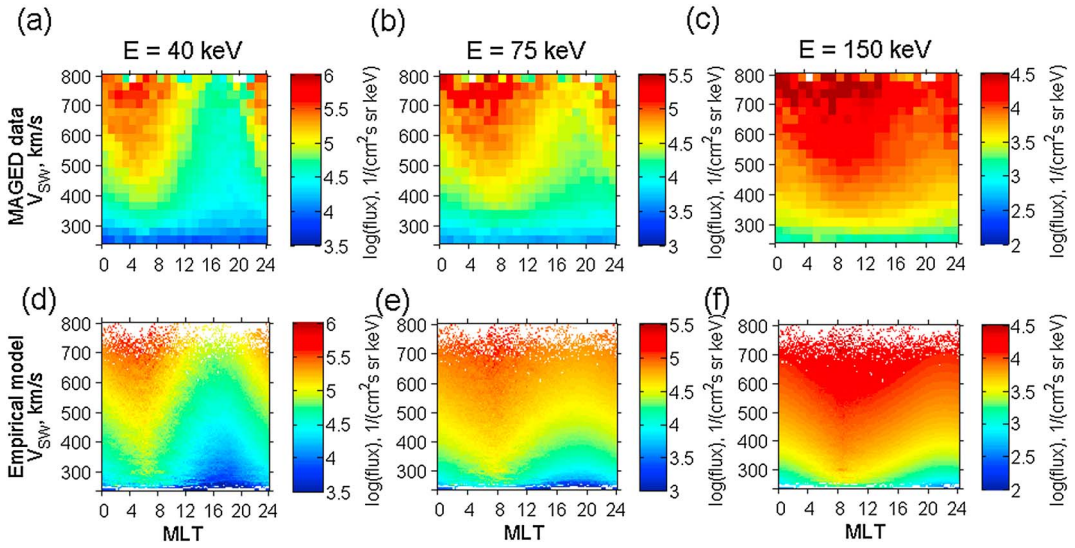


**Figure 7.** Similar to Figure 6 but with electron fluxes dependent on solar wind speed $V_{SW}$ and MLT.

## 5. Discussion and Conclusions

The geostationary satellite GOES-13 has provided a significant data set of keV range electrons with its MAGED instrument. We have analyzed five full years of that data and based on it developed an empirical model for 40, 75, and 150 keV electrons at any geostationary orbit. The developed model uses solar wind and IMF parameters as input, namely, solar wind speed and the $Z$ component of the IMF. The model reproduces well the observed electron fluxes.

The linear correlation coefficients between the MAGED electron fluxes at geosynchronous orbit and solar wind speed are (with no time delay) are from 0.30 to 0.42 (moderate correlations). The correlation coefficients between MAGED fluxes and the final, time-delayed empirical model are between 0.49 and 0.57 (stronger correlations). These correlations indicate that the solar wind speed has an effect on the electron fluxes, but it is a connection that takes place through a number of magnetospheric processes.

Employing geomagnetic indices (with significantly better correlation coefficients for the MAGED data than solar wind or IMF parameters) would likely have made the empirical model more accurate in the fluxes overall. However, our purpose in this study was to quantify and model the effect that solar wind and IMF conditions have on electron fluxes at geosynchronous orbit. Furthermore, an empirical model using solar wind and IMF parameters suits much better for forecasting purposes and is not dependent on anything but observations taken in the upstream solar wind. This together with the time delay of 1.5 h for the input parameters IMF $B_Z$ and solar wind speed makes the model usable for forecasting purposes.

A feasible method for improving the presented empirical model could be to use time averaging of the model parameters. This would mean searching for optimal delayed time ranges for the input parameters $V_{SW}$ and IMF $B_Z$. Likely, this would have to be done by MLT sectors as the delays are expected to vary significantly with the magnetospheric location (cf. Hartley et al., 2014). The method was recently applied by Dubyagin et al. (2016) for a very successful prediction model of the parameters of the magnetospheric tail.

Our statistical results on the electron low flux tail in the 30–150 keV energies showed higher occurrence of low flux events from dusk to dawn centered on local midnight and around the June solstice over the studied 5 years. Very low fluxes at geosynchronous orbit are associated with stretched magnetic fields, as the partial ring current develops during storm times (e.g., Green et al., 2004) or just prior to substorm particle injections (e.g., Loto'aniu et al., 2015), and they can also ensue after long geomagnetically quiet periods (e.g., Jaynes et al., 2015). Mechanisms associated with disparate solar wind velocity and IMF conditions can thus lead to very low fluxes at geosynchronous orbit, possibly weakening correlations with solar wind and IMF parameters. It is interesting that the low flux tails in our statistics are not symmetric with respect to June and December solstices. It may be possible that the location of GOES-13 at 75°W longitude and the positive magnetic latitude

at that position 11°N (Onsager et al., 2004) is behind the asymmetry. Further research would be advisable on these low flux phenomena.

Keeping in mind the points discussed above, our conclusions are the following:

1. Solar wind speed has a moderate correlation with the geostationary keV range electron fluxes for all MLT sectors.
2. IMF $B_Z$ has a significant influence in the 0 to 12 MLT sector where the $B_Z$ less than −5 nT leads to elevated electron fluxes in the 30–200 keV energy range.
3. Electrons with energies from 30 to 200 keV have particularly low flux periods that occur mainly in the night sector and have a clear seasonal preference.
4. The constructed empirical model can have a variety of applications from forecasting electron fluxes at geostationary or geosynchronous orbits to being an input to other models such as serving as low-energy boundary conditions for studying electron acceleration to MeV energies.

**Acknowledgments**
The original data used in this study are publicly available as follows. The directional differential fluxes of the MAGED telescopes and their pitch angles are provided in the NOAA archival data (http://satdat.ngdc.noaa.gov/sem/goes/data/new_avg/). The solar wind and interplanetary magnetic field (IMF) parameters, namely, solar wind pressure, density, speed, and temperature and IMF components are provided by the OMNIWeb service of the Space Physics Data Facility at the Goddard Space Flight Center (http://omniweb.gsfc.nasa.gov/). The projects leading to these results have received funding from the European Union Seventh Framework Programme (FP7/2007-2013) under grant agreement 606716 SPACESTORM and from the European Union's Horizon 2020 research and innovation program under grant agreement 637302 PROGRESS. N. Ganushkina thanks the International Space Science Institute in Bern, Switzerland, for their support of the international teams on "Analysis of Cluster Inner Magnetosphere Campaign data, in Application of the Dynamics of Waves and Wave-Particle Interaction within the Outer Radiation Belt" and "Ring Current Modeling: Uncommon Assumptions and Common Misconceptions." Support for N. Ganushkina at the University of Michigan was provided by the NASA research grants NNX14AF34G and NNX17AI48G. J. Rodriguez was supported by the National Centers for Environmental Information through NA15OAR4320137.

## References

Åsnes, A., Stadsnes, J., Friedel, R. W., Østgaard, N., & Thomsen, M. (2005). Medium energy pitch angle distributions during substorm injected electron clouds. *Geophysical Research Letters*, *32*, L10101. https://doi.org/10.1029/2004GL022008

Baker, D. N., Higbie, P. R., Hones Jr., E. W., & Belian, R. D. (1978). High-resolution energetic particle measurements at 6.6 $R_E$ 3. Low-energy electron anisotropies and short-term substorm predictions. *Journal of Geophysical Research*, *83*(A10), 4863–4868. https://doi.org/10.1029/JA083iA10p04863

Bame, S. J., McComas, D. J., Thomsen, M. F., Barraclough, B. L., Elphic, R. C., Glore, J. P., … Wymer, F. J. (1993). Magnetospheric plasma analyzer for spacecraft with constrained resources. *Review of Scientific Instruments*, *64*, 1026–1033. https://doi.org/10.1063/1.1144173

Birn, J., Thomsen, M. F., Borovsky, J. E., Reeves, G. D., McComas, D. J., Belian, R. D., & Hesse, M. (1998). Substorm electron injections: Geosynchronous observations and test particle simulations. *Journal of Geophysical Research*, *103*(A5), 9235–9248. https://doi.org/10.1029/97JA02635

Boyd, A. J., Spence, H. E., Huang, C-L., Reeves, G. D., Baker, D. N., Turner, D. L., … Shprits, Y. Y. (2016). Statistical properties of the radiation belt seed population. *Journal of Geophysical Research: Space Physics*, *121*, 7636–7646. https://doi.org/10.1002/2016JA022652

Chen, Y., Reeves, G. D., & Friedel, R. H. W. (2007). The energization of relativistic electrons in the outer Van Allen radiation belt. *Nature Physics*, *3*, 9. https://doi.org/10.1038/nphys655

Davis, V. A., Mandell, M. J., & Thomsen, M. F. (2008). Representation of the measured geosynchronous plasma environment in spacecraft charging calculations. *Journal of Geophysical Research*, *113*, A10204. https://doi.org/10.1029/2008JA013116

Denton, M. H., Thomsen, M. F., Jordanova, V. K., Henderson, M. G., Borovsky, J. E., Denton, J. S., … Hartley, D. P. (2015). An empirical model of electron and ion fluxes derived from observations at geosynchronous orbit. *Space Weather*, *13*, 233–249. https://doi.org/10.1002/2015SW001168

Denton, M. H., & Borovsky, J. E. (2008). Superposed epoch analysis of high-speed-stream effects at geosynchronous orbit: Hot plasma, cold plasma, and the solar wind. *Journal of Geophysical Research*, *113*, A07216. https://doi.org/10.1029/2007JA012998

Denton, M. H., Thomsen, M. F., Korth, H., Lynch, S., Zhang, J. C., & Liemohn, M. W. (2005). Bulk plasma properties at geosynchronous orbit. *Journal of Geophysical Research*, *110*, A07223. https://doi.org/10.1029/2004JA010861

Dubyagin, S., Ganushkina, N. Yu., Sillanpää, I., Runov, A., & Angelopoulos, V. (2016). Solar wind driven variations of electron plasma sheet densities and temperatures beyond geostationary orbit during storm times. *Journal of Geophysical Research: Space Physics*, *121*, 8343–8360. https://doi.org/10.1002/2016JA022947

Ganushkina, N. Y., Amariutei, O. A., Shprits, Y. Y., & Liemohn, M. W. (2013). Transport of the plasma sheet electrons to the geostationary distances. *Journal of Geophysical Research: Space Physics*, *118*, 82–98. https://doi.org/10.1029/2012JA017923

Garrett, H. B. (1981). The charging of spacecraft surfaces. *Reviews of Geophysics*, *19*(4), 577–616. https://doi.org/10.1029/RG019i004p00577

GOES N Series Data Book (2010). Prepared for NASA pursuant to contract NAS5-98069, Revision D.

Green, J. C., Onsager, T. G., O'Brien, T. P., & Baker, D. N. (2004). Testing loss mechanisms capable of rapidly depleting relativistic electron flux in the Earth's outer radiation belt. *Journal of Geophysical Research*, *109*, A12211. https://doi.org/10.1029/2004JA010579

Hanser, F. A. (2011). EPS/HEPAD calibration and data handbook (Tech. Rep. GOESN-ENG-048D). Carlisle, MA: Assurance Technology Corporation. Retrieved from http://www.ngdc.noaa.gov/stp/satellite/goes/documentation.html

Hartley, D. P., Denton, M. H., & Rodriguez, J. V. (2014). Electron number density, temperature, and energy density at GEO and links to the solar wind: A simple predictive capability. *Journal of Geophysical Research: Space Physics*, *119*, 4556–4571. https://doi.org/10.1002/2014JA019779

Horne, R. B., Thorne, R. M., Shprits, Y. Y., Meredith, N. P., Glauert, S. A., Smith, A. J., … P. M. E. Decreau (2005). Wave acceleration of electrons in the Van Allen radiation belts. *Nature*, *437*, 227–230. https://doi.org/10.1038/nature03939

Jaynes, A. N., Baker, D. N., Singer, H. J., Rodriguez, J. V., Loto'aniu, T. M., Ali, A. F., … Reeves, G. D. (2015). Source and seed populations for relativistic electrons: Their roles in radiation belt changes. *Journal of Geophysical Research: Space Physics*, *120*, 7240–7254. https://doi.org/10.1002/2015JA021234

Kellerman, A. C., & Shprits, Y. Y. (2012). On the influence of solar wind conditions on the outer-electron radiation belt. *Journal of Geophysical Research*, *117*, A05217. https://doi.org/10.1029/2011JA017253

Korth, H., & Thomsen, M. F. (2001). Plasma sheet access to geosynchronous orbit: Generalization to numerical field models. *Journal of Geophysical Research*, *106*(A12), 29,655–29,667. https://doi.org/10.1029/2000JA000373

Korth, H., Thomsen, M. F., Borovsky, J. E., & McComas, D. J. (1999). Plasma sheet access to geosynchronous orbit. *Journal of Geophysical Research*, *104*(A11), 25,047–25,061. https://doi.org/10.1029/1999JA900292

Lanzerotti, L. J., LaFleur, K., Maclennan, C. G., & Maurer, D. W. (1998). Geosynchronous spacecraft charging in January 1997. *Geophysical Research Letters*, *25*(15), 2967–2970.

Lezniak, T. W., & Winckler, J. R. (1970). Experimental study of magnetospheric motions and the acceleration of energetic electrons during substorms. *Journal of Geophysical Research*, *75*(34), 7075. https://doi.org/10.1029/JA075i034p07075

Li, W., Thorne, R. M., Ma, Q., Ni, B., Bortnik, J., Baker, D. N., … Claudepierre, S. G. (2014). Radiation belt electron acceleration by chorus waves during the 17 March 2013 storm. *Journal of Geophysical Research: Space Physics*, *119*, 4681–4693. https://doi.org/10.1002/2014JA019945

Li, X., Baker, D. N., Temerin, M., Reeves, G., Friedel, R., & Shen, C. (2005). Energetic electrons, 50 keV to 6 MeV, at geosynchronous orbit: Their responses to solar wind variations. *Space Weather*, *3*, S04001. https://doi.org/10.1029/2004SW000105

Loto'aniu, T. M., Singer, H. J., Rodriguez, J. V., Green, J., Denig, W., Biesecker, D., & Angelopoulos, V. (2015). Space weather conditions during the Galaxy 15 spacecraft anomaly. *Space Weather*, *13*, 484–502. https://doi.org/10.1002/2015SW001239

Ma, Q., Mourenas, D., Artemyev, A., Li, W., & Thorne, R. M. (2016). Strong enchancement of 10–100 keV electron fluxes by combined effects of chorus waves and time domain structures. *Geophysical Research Letters*, *43*(10), 4683–4690. https://doi.org/10.1002/2016GL069125

McComas, D. J., Bame, S. J., Barraclough, B. L., Donart, J. R., Elphic, R. C., Gosling, J. T., … Thomsen, M. F. (1993). Magnetospheric plasma analyzer: Initial 3-spacecraft observations from geosynchronous orbit. *Journal of Geophysical Research*, *98*, 13,453–13,465. https://doi.org/10.1029/93JA00726

Onsager, T. G., Chan, A. A., Fei, Y., Elkington, S. R., Green, J. C., & Singer, H. J. (2004). The radial gradient of relativistic electrons at geosynchronous orbit. *Journal of Geophysical Research*, *109*, A05221. https://doi.org/10.1029/2003JA010368

Rodriguez, J. V. (2014). GOES 13-15 MAGE/PD pitch angles, Algorithm Theoretical Basis Document, version 1.0 NOAA NESDIS NGDC. Retrieved from http://www.ngdc.noaa.gov/stp/satellite/goes/documentation.html., accessed September 10, 2014.

Rowland, W., & Weigel, R. S. (2012). Intracalibration of particle detectors on a three-axis stabilized geostationary platform. *Space Weather*, *10*, S11002. https://doi.org/10.1029/2012SW000816

Sicard-Piet, A., Bourdarie, S., Boscher, D., Friedel, R. H. W., Thomsen, M., Goka, T., … Koshiishi, H. (2008). A new international geostationary electron model: IGE-2006, from 1 keV to 5.2 MeV. *Space Weather*, *6*, S07003. https://doi.org/10.1029/2007SW000368

Shi, Y., Zesta, E., & Lyons, L. R. (2009). Features of energetic particle radial profiles inferred from geosynchronous responses to solar wind dynamic pressure enhancements. *Annales Geophysicae*, *27*, 851–859. https://doi.org/10.5194/angeo-27-851-2009

Thomsen, M. F., Denton, M. H., Lavraud, B., & Bodeau, M. (2007). Statistics of plasma fluxes at geosynchronous orbit over more than a full solar cycle. *Space Weather*, *5*, S03004. https://doi.org/10.1029/2006SW00257

Thomsen, M. F., Henderson, M. G., & Jordanova, V. K. (2013). Statistical properties of the surface-charging environment at geosynchronous orbit. *Space Weather*, *11*, 237–244. https://doi.org/10.1002/swe.20049

Stern, D. (1975). The motion of a proton in the equatorial magnetosphere. *Journal of Geophysical Research*, *80*(4), 595–599. https://doi.org/10.1029/JA080i004p00595

Turner, D. L., Fennell, J. F., Blake, J. B., Clemmons, J., Mauk, B., Cohen, I., … Burch, J. (2016). Energy limits of electron acceleration in the plasma sheet during substorms: A case study with the Magnetospheric Multiscale (MMS) mission. *Geophysical Research Letters*, *43*, 7785–7794. https://doi.org/10.1002/2016GL069691

Turner, D. L., & Li, X. (2008). Quantitative forecast of relativistic electron flux at geosynchronous orbit based on low-energy electron flux. *Space Weather*, *6*, S05005. https://doi.org/10.1029/2007SW000354

Volland, H. (1973). A semiempirical model of large-scale magnetospheric electric fields. *Journal of Geophysical Research*, *78*(1), 171–180. https://doi.org/10.1029/JA078i001p00171